Journal of Materials Chemistry A

Accepted Manuscript

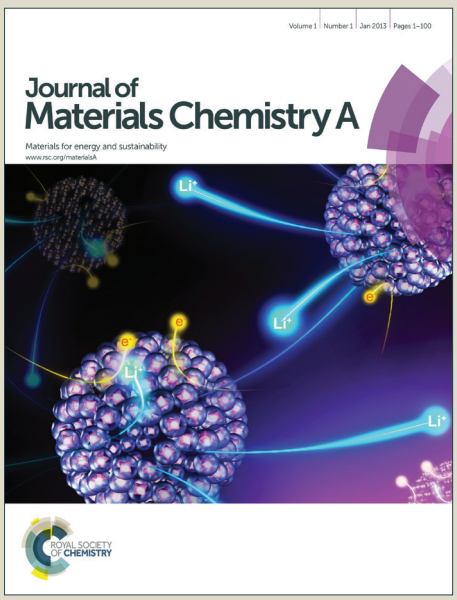

ROYAL SOCIETY OF CHEMISTRY

www.rsc.org/materialsA

Graphical Abstract:

Quasi-mesocrystal $ZnMn_2O_4$ twin-microspheres have been successfully prepared for the first time based on a distinctive oriented-attachment accompanied by Ostwald ripening.

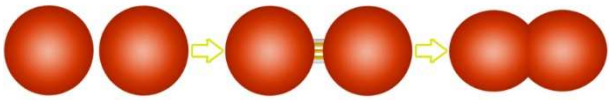

Formation of Quasi-Mesocrystal $ZnMn_2O_4$ Twin-Microspheres via an Oriented-Attachment for Lithium-Ion Batteries

Yurong Liu,[a,b] *Jing Bai,*[a] *Xiaojian Ma,*[a] *Jingfa Li,*[a] *and Shenglin Xiong*[a,c,*]

[a]*Key Laboratory of the Colloid and Interface Chemistry (Shandong University), Ministry of Education, and School of Chemistry and Chemical Engineering, Shandong University, Jinan, 250100, PR China*

[b]*School of Resources and Environmental Engineering，Shandong University of Technology, Zibo, Shandong, 255049, PR China*

[c]*CAS Key Laboratory of Materials for Energy Conversion, University of Science and Technology of China, Hefei, Anhui, 230026 (P. R. China)*

Email: chexsl@sdu.edu.cn

Abstract: Nowadays, transition metal oxides (TMOs) have generally been fabricated via annealing carbonates preobtained by precipation/solvothermal route. We noted that researchers mainly focused on how to get the expected TMOs through the calcination. However, the study about the formation process of corresponding precursors is rarely investigated. Instead, it is of much importance for the development of materials chemistry. Herein, as an example, we devise a facile polyol-based method to synthesize the quasi-mesocrystal $ZnMn_2O_4$ porous twin-microspheres for the first time. Formation chemistry and electrochemical properties of the twin-spheres have been investigated in detail. A distinctive oriented-attachment accompanied by Ostwald ripening is proposed to understand the formation of the 3D carbonate twin microspheres, providing a new research opportunity for investigating the formation of novel micro/nanostructures. Benefitting from the many unique structural advantages including quasi-mesocrystal architecture, 3D hierarchical porous microstructure, and lithium alloying reaction, the as-prepared $ZnMn_2O_4$ twin-spheres represent remarkable lithium storage properties when evaluated as anode materials for lithium-ion batteries (LIBs), with high capacity, long cycle life and remarkable rate capability. The 3D porous hierarchical structures demonstrate the great potential as anode materials for high-performance LIBs.

Keywords: twin-spheres, oriented-attachment, Ostwald ripening, lithium-ion batteries

Introduction

Nowadays, transition metal oxides (TMOs) have generally been fabricated via annealing carbonates preobtained by precipitation/solvothermal route.[1-4] We noted that researchers mainly focused on how to get the expected hollow or core-shell structures by controlling the ramp rate of temperature during the calcination. However, the study about the formation process of their respective precursors is rarely investigated. Instead, it is of much importance for the development of materials chemistry. In our work, by combination of the advantages of solvothermal/reflux avenues on engineering material structures, kinds of binary/ternary transition metal oxides micro/nanostructures have been successfully synthesized.[5-13] It should be mentioned that the growth mechanism of the corresponding precursors is studied systematically during which we got some valuable information. For example, mesoporous $ZnCo_2O_4$ twin-spheres and cubes have been selectively produced through adjusting the reactions parameters in the system of polyol solvent.[13] Based on the duration-dependent structural evolution, a brand-new crystal growth mechanism, multistep splitting then in situ dissolution-recrystallization, is first proposed, providing a new research opportunity for investigating the formation of novel micro/nanostructures.

The ever-growing energy demand has greatly stimulated recent intensive research on exploration and regulation of energy-storage devices featuring high-power and other overwhelming superiority over the existent energy carriers. Rechargeable lithium ion batteries (LIBs) have been always regarded as one of the most promising

energy-storage devices because of their many advantages, including high energy density, long lifespan and environmental benignity.[14-21] However, conventional bulk electrode materials can't overcome their inherent limits of performance and could hardly fulfill the upgrading demands for the large-scale energy applications such as electric vehicles (EVs), hybrid electric vehicles (HEVs).[22] Driven by the desire of the high-performance LIBs, great endeavor have been devoted to the development of new attractive electrode materials and engineering of the present electrode candidates.[23-25]

As a matter of fact, pioneering work by Tarascon et al.[26] has demonstrated that nanostructured TMOs can serve well as high capacity anode candidate via a conversion reaction mechanism ($MO_x+2xLi\leftrightarrow M+xLi_2O$). However, electrodes made from nanoscaled materials tend to collapse easily since they cannot be packed as densely on the current collector as micrometer-sized materials. In addition, the low tap density results in a low volumetric energy density. From the viewpoint of viable construction and energy efficiency-maximization of electrodes, a structurally optimal electrode should be a porous microstructure composed of primary nanocrystallines tightly compacted to form 3D channels for ion diffusion.[27-31] Therefore, in order to further improve the performances of LIBs, it is highly desirable to prepare materials not only consisting of nanometer-sized subunits for high specific capacity and good rate performance, but also equipped with a stable 3D porous hierarchical microstructure with remarkable ability for improving the cycling stability.

Recently, there has been much interest pertaining to the study of manganese and cobalt oxides comprising LIBs anodes because of the inherent high theoretical

capacity.[5-13, 32-46] However, cobalt based oxides are not ideal anode materials because of their high cost, toxicity, and high lithium extraction potential (2.2-2.4 V vs. Li^+/Li). In comparison, manganese oxides are nontoxic, in abundance and low cost. Furthermore, lithium extraction process can happen at as low voltage as 1.3-1.5 V over Mn-based oxides. Amongst them, $ZnMn_2O_4$ is of particular interest. The Li^+ storage over the anode can be realized through not only the conversion reaction ($ZnMn_2O_4 + 8Li^+ + 8e^- \rightarrow Zn + 2Mn + 4Li_2O$, $Zn + Li_2O \leftrightarrow ZnO + 2Li^+ + 2e^-$, and $Mn + Li_2O \leftrightarrow MnO + 2Li^+ + 2e^-$) but also the alloying reaction between Zn and Li ($Zn + Li^+ + e^- \leftrightarrow LiZn$), resulting in a high theoretical capacity of 784 mAh g^{-1}. Despite the overwhelming features, few reports track the electrochemical property of micro/nanostructured $ZnMn_2O_4$ anodes, probably due to lack of suitable synthetic methods.[41-51] Besides, both cycling performance and rate capabilities of reported $ZnMn_2O_4$ anodes need further improvement to satisfy the steady demands of high energy consumption. It is therefore imperative and necessary to exploit some efficient strategies to design novel $ZnMn_2O_4$ micro/nanostructures as high performance anodes for LIBs.

Based on the above considerations, in this article, we have devised a facile polyol-based solution method to fabricate a new type of hierarchical $ZnMn_2O_4$ micro/nanostructures. To our knowledge, this is the first report on the preparation of $ZnMn_2O_4$ porous twin-microspheres. More importantly, through examining different reaction intermediates during the synthesis, oriented-attachment accompanied by Ostwald ripening is proposed to understand the formation of the 3D carbonate twin

microspheres. In contrast to previous reports on ternary TMOs hierarchically porous electrodes from irregular self-assembly of active nanoparticles, our distinctive single-crystalline $ZnMn_2O_4$ grains were well interconnected, maintaining the same crystallographic orientation. Such hierarchical porous twin-microspheres hold many structural advantages: (i) The formation of the topical quasi-mesocrystals in the active $ZnMn_2O_4$ twin-spheres could enhance the required charge transfer and the electron conductivity during LIB operation; (ii) The uniform nanosized primary particles not only make the conversion reaction more practical but also permit the reversible formation/dissolution of solid electrolyte interphase (SEI) at the surface of the active material; (iii) The micrometer size and robust porous secondary twin-framework-microstructures can not only allow favorable penetration of electrolyte inward but also effectively buffer the collapse, aggregation, and large volume change of active materials based on the conversion reaction during the repeated discharge/charge process, maintaining the integrity of electrodes; (iv) The intrinsic properties of zinc, such as lithium alloying reaction, also contributed to the electrochemical performance. Based on the unique electrode structural features, when evaluated as an anode material for LIBs, the as-prepared hierarchically porous 3D $ZnMn_2O_4$ twin microsphere electrodes manifest excellent rate capabilities and long cycling performance, and thus display great potential as an anode material for lithium storage.

Experimental Section

Materials synthesis: In a typical synthesis of $ZnMn_2O_4$ twin-microspheres, 0.5 mmol

of $Zn(Ac)_2 \cdot 2H_2O$ and 1 mmol of $Mn(Ac)_2 \cdot 4H_2O$ are firstly dissolved into 40 mL of diethylene glycol (DEG) to form a transparent solution under magnetic stirring. Then, 30 mmol of NH_4HCO_3 powder was added to the above mixture. The resultant mixture was continually stirred until getting a homogeneous solution and then transferred into a Teflon lined stainless-steel autoclave (capacity of 50 mL). The autoclave was sealed and maintained at 200 ^oC for 20 h in an electron oven. The system was then cooled to ambient temperature naturally. The final white product, that is the $Zn_{0.33}Mn_{0.67}CO_3$ twin-microspheres, is collected and washed with water and ethanol for several times. In order to obtain the $ZnMn_2O_4$ twin-microspheres, the as-prepared $Zn_{0.33}Mn_{0.67}CO_3$ is then annealed at 600 ^oC in laboratory air for 5 h with a slow heating rate of 1 ^oC min^{-1}.

Materials Characterization: The phase of the as-synthesized samples was characterized by powder X-ray diffraction (XRD, Philips X'Pert Pro Super diffractometer, Cu Kα radiation λ = 1.54178 Å). Morphological and structural investigations were carried out with field-emission scanning electron microscopy (FESEM, JSM-6700F, JEOL). TEM images, Investigation with high-resolution analytical transmission electron microscopy (TEM and HRTEM), and energy dispersive X-ray spectroscopy (EDX) were performed on a JEM-ARM 200F atomic resolution analytical microscope operated at 200 kV. The Fourier transform infrared (FTIR) spectra were measured on a Bruker Vector-22 FT-IR spectrometer at room temperature. The TGA measurements were carried out at a heating rate of 10 ^oC min^{-1} from 20 to 800 ^oC with an air flow-rate of 100 mL min^{-1}. The measurements of the

specific surface area and the analysis of the porosity of $ZnMn_2O_4$ products were performed through measuring N_2 adsorption–desorption isotherms at 77 K, using a Micromeritics Automatic Surface Area Analyzer Gemini 2360, Shimadzu.

Electrochemical Measurements: The working electrodes were composed of the active material ($ZnMn_2O_4$ twin-spheres), conductive material (acetylene black), and polymer binder (Carboxy Methylated Cellulose, CMC,) at a weight ratio of 70:20:10 were milled for 3 h, and then coated onto the surface of a copper foil. The diameter of the electrode is 12 mm, the thickness of the coating is 200 μm and the density of the active material is about 1mg cm^{-2}. The electrochemical measurements were carried out using 2032 coin cells with lithium foil as both the counter electrode and the reference electrode. 1 M $LiPF_6$ in a mixture of ethylene carbonate (EC), dimethylcarbonate (DMC) and diethyl carbonate (DEC) (1:1:1, v/v/v) was used as the electrolyte. The cell was assembled in an Argon-filled glovebox with both the moisture and the oxygen content below 1 ppm. The galvanostatic charge/discharge measurements were carried out using CT2001A LAND Cell test system at different current densities. The cyclic voltammetry (CV) was tested in the voltage of 0.01 to 3.0 V by an electrochemical workstation (CHI760D).

Results and Discussion

Monodisperse $Zn_{0.33}Mn_{0.67}CO_3$ twin microspheres as the precursor were first synthesized through high-temperature polyol-mediated reaction (see experimental section). The morphologies of the as-prepared carbonate precursors were investigated by Field Emission Scanning Electronic Microscopy (FESEM) under different

magnifications. A panoramic FESEM image in Figure S1(a) of the Supporting Information reveals that monodisperse sphere-like structure for samples, which are at close to 100% morphological yield with average diameter about 1 μm. The corresponding high-magnification FESEM in Figure S1(b) confirms that each sphere possess an "8"-shaped structural feature. Further materials characterization with X-ray diffraction (XRD) and the thermogravimetric analysis (TGA) can be found in Supporting Information (Figure S2&3). $ZnMn_2O_4$ twin-microspheres were harvested via a topotactic conversion from $Zn_{0.33}Mn_{0.67}CO_3$ twin-microspheres in laboratory air at 600 ^oC for 5 h. With the current preparative method, it was found that the anions of the precursor salts determine the final structure of the $Zn_{0.33}Mn_{0.67}CO_3$. This offers an additional method to control product morphology. Along with the twin-spherical type of products synthesized with zinc/manganese acetate, our investigation indicates that zinc/manganese chloride as well as sulfate can only form nonuniform spherical $Zn_{0.33}Mn_{0.67}CO_3$ nanoparticles (Figure S4&5). Therefore, the morphology of our products can be finely regulated by controlling the experimental parameters.

Figure 1a depicts a typical X-ray diffraction (XRD) pattern of the final product. All diffraction peaks, within the experimental error, can be indexed to tetragonal $ZnMn_2O_4$ (JCPDS Card No. 24-1133, space group: $I4_1/amd$, $a = b = 5.720$ Å, c = 9.245 Å, $\alpha = \beta = \gamma = 90°$). No peaks of impurities were detected, indicating the high purity of the sample. The schematic crystal structure of spinel $ZnMn_2O_4$ is inserted in Figure 1a. It has a normal spinel structure wherein bivalent Zn^{2+} ions occupy the tetrahedral sites and Mn^{3+} ions center in octahedral sites in the cubic spinel structure,

which is isostructural to the spinel Co_3O_4. Energy-dispersive X-ray spectroscopy (EDS) confirms that the sample only contains Zn, Mn and O elements (Figure 1b), further confirming the formation of pure $ZnMn_2O_4$. The Mn/Zn ratio determined by EDS analysis is close 2:1, which agrees with the theoretical value.

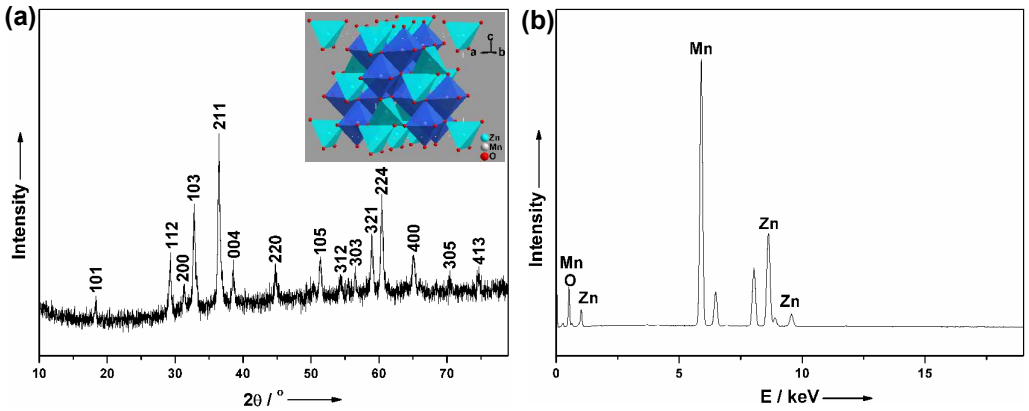

Figure 1. (a) XRD patterns of as-prepared $ZnMn_2O_4$ twin-microspheres, inset: the crystal structure of cubic spinel $ZnMn_2O_4$. (b) EDS spectrum of the twin-microspheres.

Final morphological and structural characterizations were further performed using both FESEM and TEM (HR-TEM) microscopic methods. Figure 2a displays a typical low-magnification FESEM image of the $ZnMn_2O_4$ twin-microspheres, showing a similar morphology to their corresponding precursor. The corresponding the high-magnification FESEM images in Figure 2b,c confirm that each twinned sphere still retains the pristine "8"-shaped structure with diameter of around 1.0 μm, except for a rougher exterior. Detailed structural features about $ZnMn_2O_4$ hierarchical twin spheres were further examined by TEM. Consistent with of FESEM observations, the TEM images of Figure 2d shows several typical porous $ZnMn_2O_4$ twin spheres are composed of numerous highly uniform nanosized primary nanoparticles. Figure 2f

shows a locally magnified HR-TEM image of several small nanoparticles of a $ZnMn_2O_4$ twin microsphere recorded from Figure 2e. The clear lattice spacing of 0.296 nm originates from the (112) and (-112) crystal planes with incident electron beam parallel to the zone axis of [0-21]. These several crystal grains marked by the interface curve give the impression of the relatively uniform lattice fringes, keeping the same crystallographic orientation, which is a feature of quasi-mesocrystals within a porous structure (also see Figure S6). The inset in Figure S6 describes the corresponding FFT-ED pattern with distinct diffraction spots characteristic of single-crystal, further confirming the partial-oriented growth of $ZnMn_2O_4$ crystals. In order to further explore the internal homogeneity, energy dispersive x-ray spectroscopy mapping indicated in Figure 2g offers obvious information about the element distribution within the twin spheres and the distribution of all these three elements are quite uniform throughout the whole twin-sphere, which explicitly reveals the formation of pure $ZnMn_2O_4$ products.

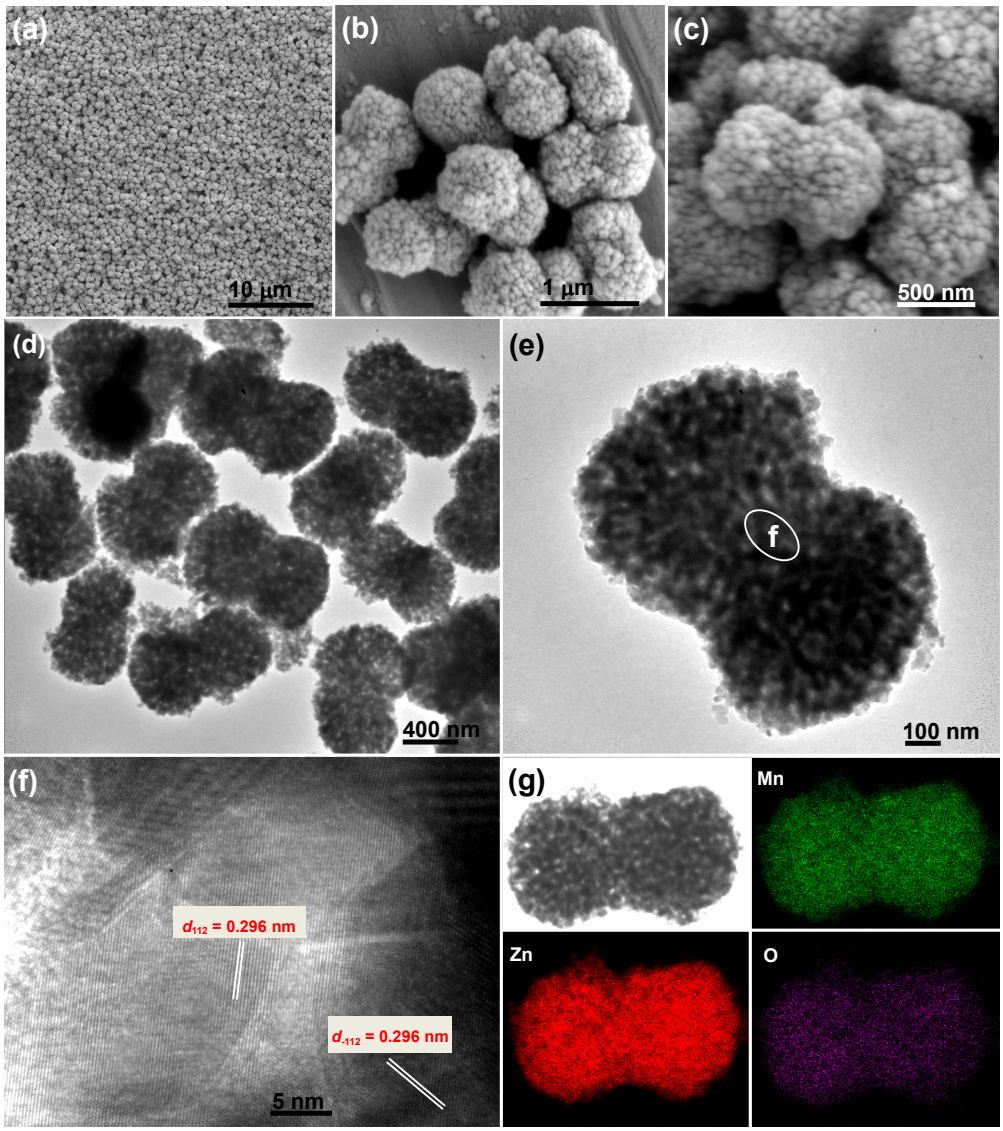

Figure 2. FESEM (a-c), TEM (d,e) and high-resolution TEM images (f) of $ZnMn_2O_4$ twin-microspheres. (g) STEM image and the corresponding EDX elemental mappings of Mn, Zn, and O for the single representative $ZnMn_2O_4$ twin-microsphere.

Further materials characterization with the specific surface areas and porous nature analysis can be found in Figure 3. The $ZnMn_2O_4$ twin-spheres exhibited the nitrogen isotherm closed to type IV with steep uptakes below P/P_0 = 0.01 and clear hysteresis loop, which showed the coexistence of micropores (< 2 nm) and mesopores (2-50 nm) in this sample. The BET surface area and pore volume of the sample was

around 20.0 m^2 g^{-1} and 0.042 cm^3 g^{-1}, respectively. The pore size distribution (PSD) curve gives a wealth of information regarding the distribution of different size pores. Here, we carried out the measurement in the range of 1.0~65 nm (Figure 3b) and analyzed it. To better understand the pore distribution of the materials, we magnified the 1.0~5 nm region (inset in Figure 3b) and found that The $ZnMn_2O_4$ twin-spheres not only had sharp peaks at less than 10 nm such as ~1.56, 1.80, 2.05, 2.32, 2.55 and 2.87 nm *et al.* but also had relatively broad ones at 9.57, 12.26, 16.61 and 36.10 nm, indicating the coexistence of hierarchical micropores and mesopores in the $ZnMn_2O_4$ twin-spheres, which make the $ZnMn_2O_4$ twin-microspheres a possible promising candidate for electrode materials of LIBs.

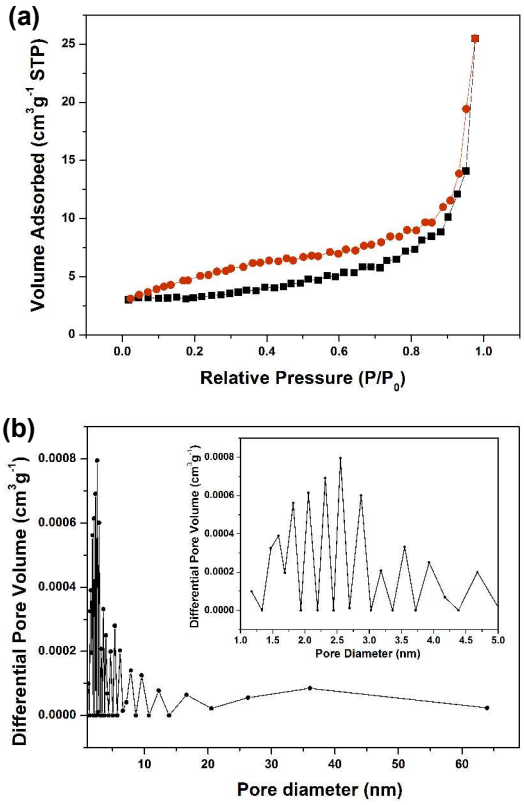

Figure 3. (a) Nitrogen adsorption-desorption isotherms and (b) pore size distribution (inset: magnified 0-5 nm region) of $ZnMn_2O_4$ twin-microspheres.

In our synthesis, the studies on the precursor elaborated that $Zn_{0.33}Mn_{0.67}CO_3$ morphology was found to be dependent strongly on reaction parameters such as the anions of the precursor salts and the reaction time. To shed more light on the growth mechanism of $Zn_{0.33}Mn_{0.67}CO_3$ twin-spheres, we quenched the precursor $Zn_{0.33}Mn_{0.67}CO_3$ at different reaction stages to investigate the microstructural features. Time-dependent experiments in Figure 4 display that the morphology of carbonate phase evolves significantly upon the reaction time, transforming from individual sphere-like nanoparticles gradually to intercoupling-spherical nanoparticles, and finally to twin-spheres. The specified evolution is also reflected in terms of the phase detection by XRD patterns shown in Figure S7 (see Supporting Information). $Zn_{0.33}Mn_{0.67}CO_3$ was confirmed to form within 10 min and the products have become better crystallinity with the elongation of reaction time in the present synthetic system. The detailed microstructural textures can supply growth mechanism information underlying the shape evolution. The SAED image of Figure S8c in Supporting Information, taken out of the area marked in a single twin-sphere of Figure S8a, holds the arc-diffraction pattern rather than single spots or ring-patterned fashion, testifying the locally preferred orientation growth. Moreover, various crystal grains in HRTEM images of Figure S8d&e show uniform lattice fringes with very little deviation, complying with the observation over ED, wherein the d-spacings of 0.284 nm and 0.224 nm are designed to be (104) and (-1-13) crystal planes. Therefore, it can be reasonably concluded that the observed coupling process carried out through a "distinctive oriented-attachment" of two partnership spheres along the direction

normal to the (104) crystal planes. On the other hand, the newborn nanoparticles in the initial stage have high surface energy due to a large amount of dangling atoms exposed outside (shown by red arrows in Figure 4a). Driven by energy minimization, these nanoparticles tend to dissolve-recrystallize to the surface of the larger size particle. As a result, by the synergetic function of distinctive oriented attachment and Ostwald ripening, the final twin-spheres became elongated after the coupling process compared to their perfect intermediate spheres.

In order to understand the role of DEG in the above constructional process, we have tried using monohydric alcohol (CH_3CH_2OH) or other polyol ($HOCH_2CH_2OH$) to conduct the same experiments under identical conditions; however, no $Zn_{0.33}Mn_{0.67}CO_3$ twin-spheres could be obtained (Figure S9&10). The fingerprint absorption characteristics of DEG can be detected in the $Zn_{0.33}Mn_{0.67}CO_3$ twin-spheres by FTIR spectroscopy (Supporting Information, Figure S11). In this regard, the introduction of DEG herein should be ascribed to the beneficial adsorption of CH_2- and OH- groups on $Zn_{0.33}Mn_{0.67}CO_3$ surfaces. The bidentate DEG with appropriate polarity is believed to play a crucial role in bringing the $Zn_{0.33}Mn_{0.67}CO_3$ building units together. In particular, DEG could work as a linear linker to bridge two $Zn_{0.33}Mn_{0.67}CO_3$ spheres. Accompanied by Ostwald ripening via the expense of the small nanoparticles, the contact probability of the $Zn_{0.33}Mn_{0.67}CO_3$ spheres is enhanced, resulting in further fusion between the intercoupling two $Zn_{0.33}Mn_{0.67}CO_3$ spheres, as shown in the color illustration in Figure 3.

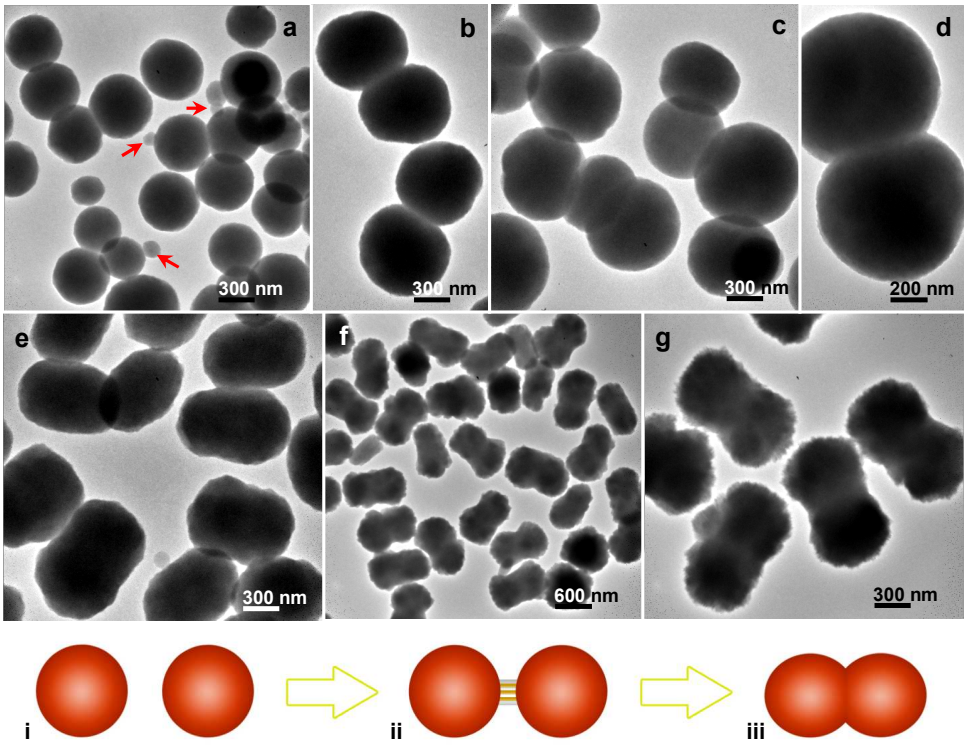

Figure 4. TEM images of the precursors synthesized at 200 ºC for 10 min (a,b); 15 min (c,d); 20 min (e); 1 h (f); and 2 h (g). Color illustration indicates the coupling process: (i) randomly oriented spheres, (ii) alignment between two spheres with assistance of DEG ligands (yellow thin lines between two spheres), and (iii) formation of $Zn_{0.33}Mn_{0.67}CO_3$ twin-microspheres.

Figure 5a indicates the cyclic voltammetry (CV) curves of the first three cycles of the mesocrystal $ZnMn_2O_4$ Twin-Microsphere electrode under a current density of 0.5 A g^{-1} and cycled between 0.01 and 3 V vs Li^+/Li. During the first cathodic scan, two peaks can be observed. The broad peak at ~1.23 V could be attributed to the reduction of Mn^{3+} to Mn^{2+}, and the intense peak at ~0.19 V can be ascribed to the reduction of Mn^{2+} and Zn^{2+} to metallic Mn and Zn embedded into a Li_2O matrix, followed by the alloying reaction of Zn with Li to form LiZn, which is consistent with that reported in

literature.[41-46] While the minor peak at ~0.98 V could be ascribed to the irreversible decomposition of the solvent in the electrolyte to form the solid-electrolyte interface (SEI). During the first charging process, the strong peak at 1.3 V and broad peak at 1.57 V correspond to the oxidation of Mn^0 to Mn^{2+} and the oxidation of Zn^0 to Zn^{2+}, respectively, along with the decomposition of the Li_2O matrix. From the second cycle onward, the CV curves show two pairs of obvious redox peaks. The one at around 0.46/1.3 V corresponds to the reduction/oxidation of MnO, while the other one at around 0.85/1.6 V corresponds to o the reduction/oxidation of ZnO. Furthermore, the CV curves of the second and third cycles almost overlap, implying an excellent cyclability of the $ZnMn_2O_4$ twin-microsphere electrode. Meanwhile, the correlative plateau regions can be observed in the initial three and 50th charge/discharge profiles of the $ZnMn_2O_4$ Twin-Microsphere electrode (Figure 5b).

Figure 5c shows cycling performance of the $ZnMn_2O_4$ twin-microsphere electrode under a current density of 0.5 A g^{-1} in the voltage range of 0.01-3 V vs Li^+/Li. The initial charge and discharge capacities of the $ZnMn_2O_4$ twin-microsphere electrode are 732 and 1106 mA h g^{-1}, respectively, corresponding to a Coulombic efficiency (CE) of 66%. The ca. 34% capacity loss of the $ZnMn_2O_4$ twin-microsphere electrode can be mainly ascribed to the formation of the SEI. Starting from the second cycle, the CE increases to more than ~99% and meanwhile the reversible capacity of $ZnMn_2O_4$ twin-microspheres gradually increases to 815 mA h g^{-1} after 70 cycles. Moreover, the high reversible capacity of 860 mA h g^{-1} for the $ZnMn_2O_4$ twin-microsphere electrode was still retained after 130 cycles (Figure 5c). The increasing trend of the capacity of

$ZnMn_2O_4$ twin-microspheres in the initial 70 cycles is likely due to the reversible growth of the polymeric gel-like film originating from the kinetically activated electrolyte degradation as well as gradual formation of SEI over the inner active nanoparticles. Not all the surface layer is covered on the first discharge. The internal surface within the pores is more difficult to access. It would appear that the polymer layer establish slowly, over considerable cycles, which has been often observed in other metal oxide composites in some pioneering literature.[46,53-55]

To further probe the electrochemical performance of $ZnMn_2O_4$ twin-microspheres electrode, we investigated its rate capability (Figure 5d). As expected, $ZnMn_2O_4$ twin-microspheres represented an excellent rate capability compared with almost all documents reported about $ZnMn_2O_4$ micro/nanostructures and $ZnMn_2O_4$-based Composite structures.[41-52] As the current densities increase from 0.2 to 0.5, 1, and 2 A g^{-1}, the electrode shows e capacity retention, varying from 772 to 695, 618, and 484 mA h g^{-1}, respectively. When the rate was further increased to 5 A g^{-1}, $ZnMn_2O_4$ twin-microspheres still delivered a favorable capacity of 329 mA h g^{-1}. Remarkably, when the rate turns back to 0.2 A g^{-1}, the capacity can be retained as high as 1084 mA h g^{-1} even more than 190 cycles without any loss and the Coulombic efficiency is almost 100% (see Figure 5e). It should be mentioned that when the current density was returned from 5.0 to 0.2 A g^{-1}, the discharge capacity of $ZnMn_2O_4$ twin-microspheres electrode more than 190 cycles (1084 mA h g^{-1}) is higher than that (772 mA h g^{-1}) of the initial performance at 0.2 A g^{-1}. Such activation phenomenon is possibly originate from the gradual formation of the SEI due to the postponed

penetration of the electrolytes into the inner part of active nanoparticles in the 3D porous architecture and then results in the increase of capacity. Of course, the specific reasons need to be studied further. Such phenomenon has also been reported by other researchers.[56]

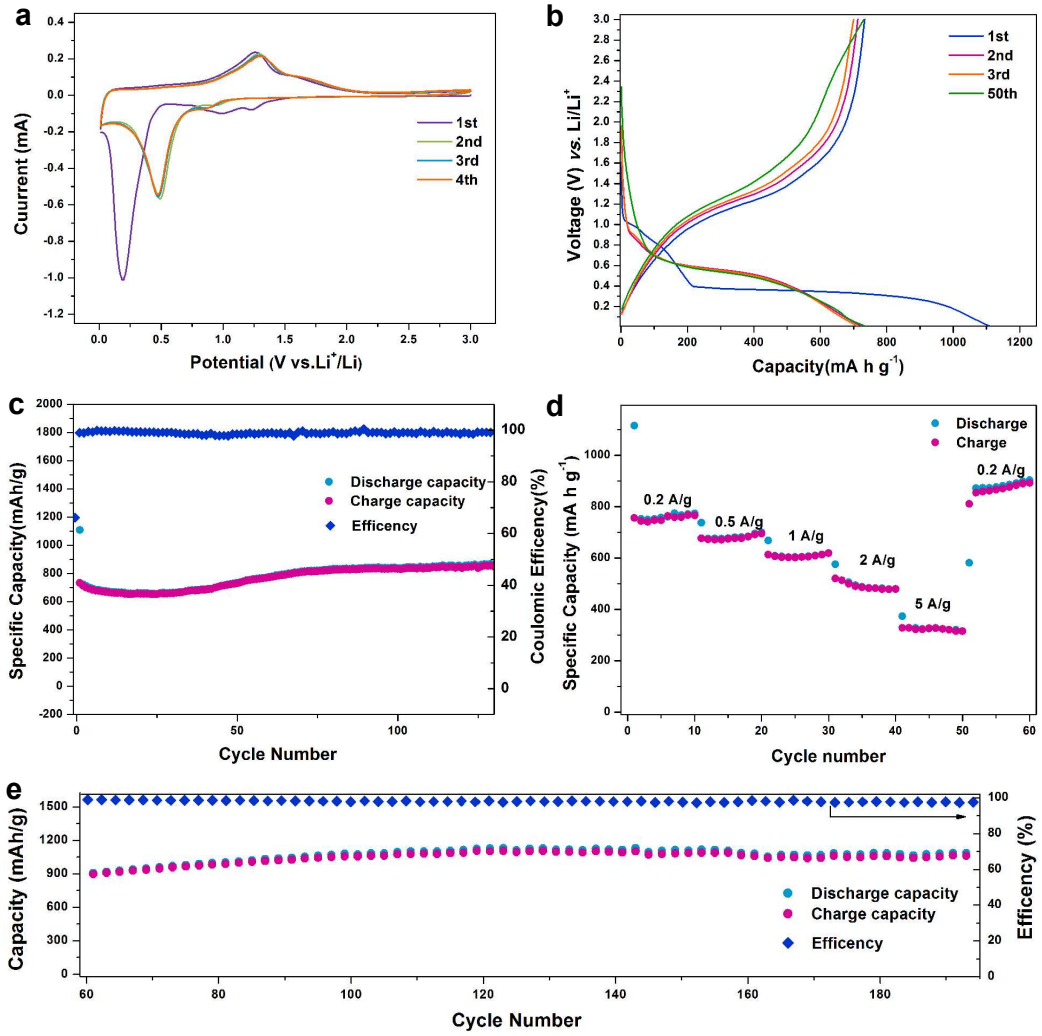

Figure 5. (a) Cyclic voltammetry (CV) curves for the as-fabricated $ZnMn_2O_4$ twin microspheres at a scan rate of 0.1 mV s^{-1} in the voltage window of 0.01–3.0 V. (b) Charge–discharge curves of $ZnMn_2O_4$ twin microspheres at a current density of 0.5 A g^{-1}. (c) Cycling performance of $ZnMn_2O_4$ twin microspheres at a current of 0.5 A g^{-1}. (d) Cycling performance of $ZnMn_2O_4$ twin microspheres at various rates. (e) The cycling performance of $ZnMn_2O_4$ twin microspheres after the rate test.

The above results unambiguously confirm a high specific capacity, superior cycling stability, and excellent rate performance of the $ZnMn_2O_4$ twin-microspheres electrode, which can be attributed to our rationally designed 3D porous architecture with many structural advantages. On the one hand, the unique 3D porous hierarchical configuration composed of numerous primary nanoparticles can afford more active sites for Li^+ ions access and regulates the stress induced by the volume change during the repeated Li ions insertion/extraction, thus resulting in a higher efficiency of the lithiation and delithiation process. The porosity on the surface and interior can further provide a short pathway for lithium ions diffusion and thus improves the rate capability. On the other hand, the generation of crystallographically oriented mesocrystals in the active $ZnMn_2O_4$ phases could also be beneficial to charge transfer and electron conductivity during battery operation. Nevertheless, the intrinsic properties of zinc, such as lithium alloying reaction, also contributed to the electrochemical performance.

Conclusions

In summary, this work is significant in the following aspects. First, it expands the research space of material chemistry, offering a new research opportunity for investigating the formation of novel micro/nanostructures. Second, it demonstrates new possibility to employ the solution-based synthesis to prepare novel complex hierarchical structures. And third, is serves as a model example to couple two individual spheres to quasi-mesocrystal twin-spheres based on a distinctive oriented-attachment accompanied by Ostwald ripening. As investigated above, this

new type of hierarchical architecture possess many structural merits, including quasi-mesocrystal architecture, porous, 3D hierarchical microstructure composed of numerous primary active nanopaticles, and lithium alloying reaction. When applied as anode material in LIBs, $ZnMn_2O_4$ twin-spheres exhibited high rate capabilities, and long-term cycling stability without capacity decay. Our synthetic strategy may be extended to other electrode materials that experience poor electron/Li ion transfer kinetics and SEI instability caused by large volume change.

Acknowledgements

The authors gratefully acknowledge the financial supports provided by the National Basic Research Program of China (the 973 Project of China, No. 2011CB935901), National Natural Science Fund of China (No. 21371108), Shandong Provincial Natural Science Foundation for Distinguished Young Scholar (No. JQ201304), the Independent Innovation Foundations of Shandong University (No. 2012ZD008), the National Science Foundation of Shandong Province (No. ZR2012BM018), start-up funding for new faculty in Shandong University, China Postdoctoral Science Foundation (No. 2013M541904), and the Opening Project of CAS Key Laboratory of Materials for Energy Conversion (No. KF2014002).

References

1 L. Zhang, D. Y. Zhao, X. W. Lou, *Adv. Mater.* **2012**, *24*, 745-748.

2 C. C. Li, X. M. Yin, T. H. Wang, H. C. Zeng, *Chem. Mater.* **2009**, *21*, 4984-4992.

3 H. P. Cong, S. H. Yu, *Cryst. Growth Des.* **2009**, *9*, 210-217.

4 L. H. Hu, Q. Peng, Y. D. Li, *J. Am. Chem. Soc.* **2008**, *130*, 16136-16137.

5 S. L. Xiong, C. Z. Yuan, X. G. B. J. Xi, Y. T. Qian, *Chem. Eur. J.* **2009**, *15*, 5320-5326.

6 S. L. Xiong, J. S. Chen, X. W. Lou, H. C. Zeng, *Adv. Funct. Mater.* **2012**, *22*, 861-871.

7 J. F. Li, S. L. Xiong, X. W. Li, Y. T. Qian, *Nanoscale* **2013**, *5*, 2045-2054.

8 J. F. Li, S. L. Xiong, Y. R. Liu, Z. C. Ju, Y. T. Qian, *ACS Appl. Mater. Interfaces* 2013, *5*, 981-988.

9 J. F. Li, S. L. Xiong, X. W. Y. T. Qian, *J. Mater. Chem.* **2012**, *22*, 23254-23259.

10 J. F. Li, J. Z. Wang, X. Liang, Z. J. Zhang, H. K. Liu, Y. T. Qian, S. L. Xiong, *ACS Appl. Mater. Interfaces* **2014**, *6*, 24-30.

11] J. F. Li, J. Z. Wang, D. Wexler, D. Q. Shi, J. W. Liang, H. K. Liu, S. L. Xiong, Y. T. Qian, *J. Mater. Chem. A* **2013**, *1*, 15292-15299.

12 J. F. Li, S. L. Xiong, Y. R. Liu, Z. C. Ju, Y. T. Qian, *Nano Energy* **2013**, *2*, 1249-1260.

13 J. Bai, X. G. Li, G. Z. Liu, Y. T. Qian, S. L. Xiong, *Adv. Funct. Mater.* **2014**, *24*, early view.

14 P. G. Bruce, B. Scrosati and J.M. Tarascon, *Angew. Chem., Int. Ed.* **2008**, *47*, 2930.

15 J. B. Goodenough and Y. Kim, *Chem. Mater.* **2010**, *22*, 587-603.

16 V. Etacheri, R. Marom, R. Elazari, G. Salitra and D. Aurbach, *Energy Environ. Sci.* **2011**, *4*, 3243-3262.

17 P. G. Bruce, S. A. Freunberger, L. J. Hardwick and J. M. Tarascon, *Nat. Mater.* **2012**, *11*, 19-29.

18 Z. Y. Wang, L. Zhou and X. W. Lou, *Adv. Mater.* **2012**, *24*, 1903-1911.

19 F. Y. Cheng, J. Liang, Z. L. Tao and J. Chen, *Adv. Mater.* **2011**, *23*, 1695-1715.

20 H. Q. Li and H. S. Zhou, *Chem. Commun.* **2012**, *48*, 1201-1217.

21 Y. Li, Z. Y. Fu and B. L. Su, *Adv. Funct. Mater.* **2012**, *22*, 4634-4667.

22 A. S. Arico, P. Bruce, B. Scrosati, J. M. Tarascon and W. Van Schalkwijk, *Nat. Mater.* **2005**, *4*, 366-377.

23 N. S. Choi, Z. H. Chen, S. A. Freunberger, X. L. Ji, Y. K. Sun, K. Amine, G. Yushin, L. F. Nazar, J. Cho and P. G. Bruce, *Angew. Chem., Int. Ed.* **2012**, *51*, 9994-10024.

24 J. B. Goodenough and K. S. Park, *J. Am. Chem. Soc.* **2013**, *135*, 1167-1176.

25 L. W. Ji, Z. Lin, M. Alcoutlabi and X. W. Zhang, *Energy Environ. Sci.* **2011**, *4*, 2682-2699.

26 P. Poizot, S. Laruelle, S. Grugeon, L. Dupont, J-M. Tarascon, *Nature* **2000**, *407*, 496-499.

27 L. Zhou, D. Y. Zhao, X. W. Lou, *Angew. Chem. Int. Ed.* **2012**, *51*, 239-241.

28 G. X. Wang, H. Liu, J. Liu, S. Z. Qiao, G. Q. Max Lu, P. Munroe, H. Ahn, *Adv. Mater.* **2010**, *22*, 4944-4948.

29 J. Liu, T. E. Conry, X. Y. Song, M. M. Doeff, T. J. Richardson, *Energy Environ. Sci.* **2011**, *4*, 885-888.

30 Y. K. Sun, S. M. Oh, H. K. Park, B. Scrosati, *Adv. Mater.* **2011**, *23*, 5050-5054.

31 O. K. Park, Y. Cho, S. Lee, H. Yoo, H.-K. Song, J. Cho, *Energy Environ. Sci.* **2011**, *4*, 1621-1633.

32 M. V. Reddy, G. V. Subba Rao, B. V. R. Chowdari, *Chem. Rev.* **2013**, *113*, 5364-5457.

33 X. W. Lou, D. Deng, J. Y . Lee, J. Feng, L. A. Archer, *Adv. Mater.* **2008**, *20*, 258-262.

34 Y. G. Li, B. Tan, Y. Y. Wu, *Nano Lett.* **2008**, *8*, 265-270.

35 X. Y. Yang , K. C. Fan, Y. H. Zhu, J. H. Shen, X. Jiang, P. Zhao, S. R. Luan, C. Z. Li, *ACS Appl. Mater.*

Interfaces **2013**, *5*, 997-1002.

36 W. Luo, X. L. Hu, Y. M. Sun, Y. H. Huang, *ACS Appl. Mater. Interfaces* **2013**, *5,* 1997-2003.

37 S. Nayak, S. Malik, S. Indris, J. Reedijk, A.K. Powell, *Chem. Eur. J.* **2010**, *16*, 1158-1162.

38 J. C. Guo, Q. Liu, C. S. Wang, M. R. Zachariah, *Adv. Funct. Mater.* **2012**, *22*, 803-811.

39 H. Xia, M.O. Lai, L. Lu, *J. Mater. Chem.* **2010**, *20*, 6896-6902.

40 C. Chae, J. H. Kim, J. M. Kim, Y. K. Sun, J. K. Lee, *J. Mater. Chem.* **2012**, *22*, 17870-17877.

41 Y. Y. Yang, Y. Q. Zhao, L. F. Xiao and L. Z. Zhang, *Electrochem. Commun.* **2008**, *10*, 1117-1120.

42 L. F. Xiao, Y. Y. Yang, J. Yin, Q. Li and L. Z. Zhang, J. *Power Sources* **2009**, *194,* 1089-1093.

43 Y. F. Deng, S. D. Tang, Q. M. Zhang, Z. C. Shi, L. T. Zhang, S. Z. Zhan and G. H. Chen, J. *Mater. Chem.* **2011**, *21*, 11987-11995.

44 F. M. Courtel, H. Duncan, Y. Abu-Lebdeh and I. J. Davidson, *J. Mater. Chem.* **2011**, *21*, 10206-10218.

45 L. Zhou, H. B. Wu, T. Zhu, X. W. Lou, *J. Mater. Chem.* **2012**, *22*, 827-829.

46 G. Q. Zhang, L. Yu, H. B. Wu, H. E. Hoster, X.W. Lou, *Adv. Mater.* **2012**, *24*, 4609-4613.

47 J. Zhao, F. Q. Wang, P. P. Su, M. R. Li, J. Chen, Q. H. Yang, C. Li, *J. Mater. Chem.* **2012**, *22*, 13328-13333.

48 P. F. The, Y. Sharma, Y. W. Ko, S. S. Pramana, M. Srinivasan, *RSC Adv.* **2013**, *3*, 2812-2821.

49 Z. C. Bai, N. Fan, C. H. Sun, Z. C. Ju, C. L. Guo, J. Yang, Y. T. Qian, *Nanoscale* **2013**, *5*, 2442-2447.

50 C. Z. Yuan, J. Y. Li, L. R. Hou, L. H. X. G. Zhang, *Part. Part. Syst. Charact.* **2014**, DOI: 10.1002/ppsc.201300338.

51 L. W. Yin, Z. W. Zhang, Z. Q. Li, F. B. Hao, Q. Li, C. X. Wang, R. H. Fan, Y. X. Qi, *Adv. Funct. Mater.* **2014**, DOI: 10.1002/adfm.201400108.

52 N. N. Wang, X. J. Ma, H. Y. Xu, L. Chen, J. Yue, F. E. Niu, J. Yang, Y. T. Qian, *nano Energy* **2014**, *6*, 193-199.

53 S. Laruelle, S. Grugeon, P. Poizot, M. Dolle, L. Dupont, J. M. Tarascon, *J. Electrochem. Soc.* **2002**, *149*, A627-A634.

54 J. S. Do, C. H. Weng, *J. Power Sources* **2005**, *146*, 482-486.

55 Y. Y. Yang, Y. Q. Zhao, L. F. Xiao, L. Z. Zhang, *Electrochem. Commun.* 2008, *10*, 1117-1120.

56 G. M. Zhou, D. W. Wang, F. Li, L. L. Zhang, N. Li, Z. S. Wu, L. Wen, G. Q. Lu, H. M. Cheng, *Chem. Mater.* **2010**, *22*, 5306-5313.